# Simulation of Transonic Viscous Flow over a Fighter-Like Configuration Including Inlet

Jolen Flores,* Neal M. Chaderjian,* and Reese L. Sorenson*
*NASA Ames Research Center, Moffett Field, California*

**The simulation of transonic viscous flow over a modified F-16A including inlet is presented. A zonal approach is utilized that allows appropriate clustering suitable for viscous calculations on all solid surfaces. Computational efficiency is enhanced by solving the thin-layer Navier-Stokes equations in viscous zones adjacent to the aircraft and the Euler equations on those coarse zones away from the aircraft. The flow conditions for this transonic case are $M_\infty = 0.9$, $\alpha = 4.12$ deg, and a Reynolds number based on root chord of $4.5 \times 10^6$. A total of 19 zones are utilized yielding a total of 351,000 grid points. This case required about 3000 iterations to reduce the residual by three orders, which takes about 10 h of CPU time on the current NASA Ames supercomputer. Pressure distributions on the wing and on cross sections through the inlet region compare favorably with the experimental data for this transonic case.**

## Introduction

WITH the advent of supercomputers and the maturation of numerical procedures, it is now possible to solve three-dimensional Euler and Navier-Stokes equations at reasonable computer costs. This is because of the fast vector processing available in these computers and the improvement of existing computational fluid dynamic (CFD) algorithms.

Prior to the arrival of supercomputers, the use of the time-accurate Navier-Stokes equations for transonic flow had been primarily limited to simple-geometry, high-speed types of flows. These include the work of Holst et al.,[1] Hung,[2,3] Shang,[4] and Pulliam and Steger.[5] More recently, a few transonic applications involving more sophisticated geometries have appeared including those of Deiwert and Rothmund,[6] Deiwert et al.,[7] Fujii and Kutler,[8] and Mansour.[9] However, even those solutions were conducted on coarse grids and required large amounts of CPU time, which precluded their use for more complicated geometries.

Codes that can predict the flow physics over complex and realistic geometries are currently under development. The successful linear or nonlinear potential methods are no longer sufficient to meet the demands imposed by the aircraft industry. In order to simulate accurately the flow physics arising from such phenomena as store separation, multiple lifting-surface interactions, and flutter and buffet calculations involving comples boundary-layer flow requires the solution of the Navier-Stokes equations. However, to fully exploit the Navier-Stokes equations and the fluid physics they reveal, high-grid resolution is required. High-grid resolution translates into large storage demands, which tax existing supercomputers. Couple this with the grid-generation problem over complicated geometries, and a formidable challenge is realized. Fine-grid Navier-Stokes solutions have been obtained over wings, wing/fuselage, and transport-type aircraft.[10-12] However, these geometries have been simple and have avoided the grid-generation problem associated with complicated geometries. Thus, it is still a challenge to obtain fine-grid viscous solutions over a complicated geometry.

Not all aircraft companies have access to large memory supercomputers, so the problem of storage space still remains. To overcome the storage problem, zonal approaches have become increasingly popular. Zonal approach means the partitioning of the flowfield into distinct "zones," each of which is solved independently.

The zonal approach has a number of advantages. First, it mitigates the difficulty of generating three-dimensional grids for different types of complex configurations with appropriate clustering to capture high-gradient flow physics; it is this grid-generation difficulty that has probably been the single biggest reason for the slow development of three-dimensional CFD applications about complex geometries.[13]

Second, zonal methods allow different types of grid topologies to be used to improve mesh efficiency; that is, more points are used on the configuration where accuracy is desired, and fewer points are used away from the configuration where flow gradients are small. The zonal concept has been successfully applied to the full-potential equations[14,15] and to the Euler equations.[16,17] It is also possible with the zonal approach to solve different equation sets in different zones.[18]

The idea of solving the Euler and Navier-Stokes equations within the framework of zonal methods has been realized through the development of the transonic Navier-Stokes (TNS) code that is used in this present paper. The ultimate goal of the TNS code is to be able to predict the transonic viscous flow over the complete F-16A fighter aircraft. The F-16A was chosen because experimental data exist for code validation, it is a complicated geometry, and its flowfield involves complicated fluid physics. With all the slope discontinuities that exist in this geometry, appropriate clustering on the entire geometry is extremely difficult with a single grid. Through a series of steps the TNS code was first developed to compute transonic flow over isolated arbitrary wing geometries with both free-air and wind-tunnel-wall boundary conditions. For the wing code, the method utilized a zonal approach with a total of four grid zones.[19,20] The code was then extended to a 16-zone TNS wing-fuselage code. In particular, the code was used to solve transonic viscous flow over a modified (faired-over inlet and no tail assembly) F-16A.[21,22] It should be mentioned that the combination of zonal methods and the solution of the Euler equations has been successful when used on complex geometries[23] and to solve the complete F-16A aircraft.[24] However, to the best of the authors' knowledge, this is the first successful implementation of the three-dimensional Euler and Navier-Stokes equations in a zonal approach for a complex aircraft. The governing equation, numerical algorithm, and other details of the TNS procedure can be found in Refs. 19–22, and are thus

Presented as Paper 87-1199 at the AIAA 19th Fluid Dynamics, Plasma Dynamics and Laser Conference, Honolulu, HI, June 8-10, 1987; received June 23, 1987; revision received Sept. 24, 1987. 

*Research Scientist. Member AIAA.

not repeated here. The current work reflects the extension of the TNS code to include the inlet and diverter regions. This paper will focus on the modifications required of the zoner and flow solver routines and the examination of the flow physics, as well as experimental validation, around the diverter region.

## Zonal Philosophy

### F-16A Geometry and Base Grid

The modified F-16A is shown in Fig. 1, illustrating the exclusion of the tail assembly. Note that the forebody, canopy, leading-edge strake, wing, shelf regions, inlet, and diverter sections are unmodified and are of the exact F-16A geometry. Figure 2 shows an expanded view of the inlet and diverter sections. The diverter plate is a vertical extension that displaces the inlet from the fuselage in order to prevent the fuselage boundary layer from being ingested into the inlet. There are some problems associated with determining how to grid these regions. The main problem is in the geometry itself, particularly in the way the aft part of the diverter plate merges into the fuslage body. This causes the grid cells associated with the diverter section to collapse into wedges. Fortunately, a no-slip boundary condition is applied at this location, and this seems to suppress any numerical problems that may arise due to this grid singularity. It is extremely difficult to achieve appropriate clustering at all solid boundaries for this complicated geometry with a single grid. However, with the use of zonal methods, this becomes a manageable problem. To initiate the inlet code, a base grid about the geometry is supplied as input. The base grid was generated via an elliptic method.[25] The polar type of topology about the fuselage can be seen in Fig. 3. This polar grid collapses into a singular line in front of the fuselage nose. However, this causes no problem in the flow solver because of the averaging of the dependent variables about this singularity. A chordwise slice through the wing would reveal an H-mesh type of local topology.

The base grid is fed into a zonal routine, which subsequently creates 16 zones by subdividing the original base grid. Through certain parameters in the zonal routine, the zones created are essentially of three types: a) inviscid zones, b) viscous zones with clustering on one face of the zone for wing or fuselage surfaces, and c) viscous zones with clustering on two adjacent faces of the zone for the wing/fuselage juncture regions. An additional three blocks were required to model the inlet/diverter sections, yielding a total of 19 zones.

### Inlet and Diverter Zones

Figure 4 shows the actual zoned grids about a portion of the F-16A where the inlet and diverter are located. The red grid denotes zone 1, also referred to as the outer grid, which has viscous clustering normal to the fuselage surface. A brief explanation is required to better understand the placement of the grids for the inlet and diverter sections. The grid for the diverter section begins at the same streamwise plane as the face of the inlet and extends back to where the diverter merges into the fuselage body. A single grid in this region would suffice for a flow solver; however, this would require a clustering routine that could handle clustering on three solid surfaces, the underbelly of the fuselage, the diverter plate, and the upper surface of the inlet. To reduce modifications required for the zonal (as well as the flow solver) routine, it was decided to exploit the current capabilities of these routines to handle the wind/fuselage junction region, i.e., clustering on two adjacent faces. Therefore, two grids were constructed in the diverter section—an upper diverter grid and a lower diverter grid—each having two no-slip surfaces and a common boundary plane perpendicular to the diverter plate. This greatly simplified the modifications required for both previously mentioned routines. The outer boundary of the lower diverter grid is denoted by the color green, and that of the upper diverter by the color yellow. The beginning of the inlet grid is at the fuselage underbelly, at a streamwise location about where the strake begins to protrude. The inlet grid ends right at the face of the inlet, and coincides with the diverter grids at a common boundary plane. The outer boundary of the inlet grid is denoted by the light blue color. Previously, these outer boundaries, which coincide with boundary planes of zone 1, were treated as no-slip surfaces for the faired-over inlet case. For the current case, they are no longer treated as no-slip surfaces, but rather as zonal

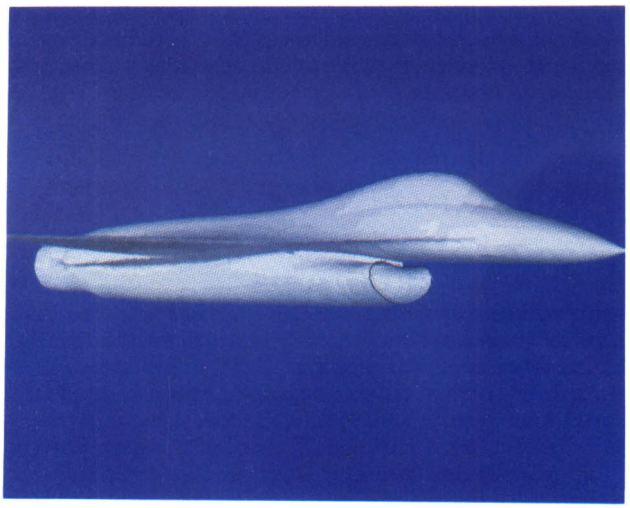

Fig. 1 F-16A modified geometry.

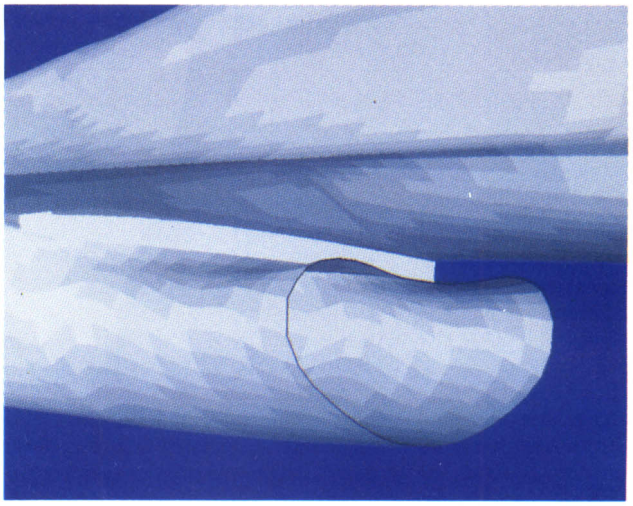

Fig. 2 Expanded view of F-16A inlet-diverter sections.

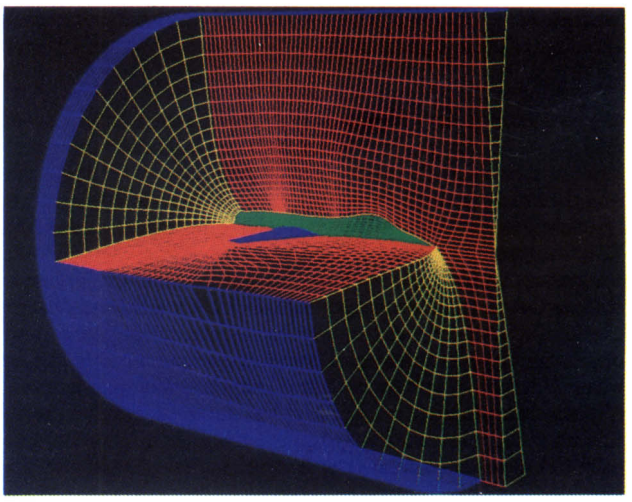

Fig. 3 Base grid about F-16A modified geometry.

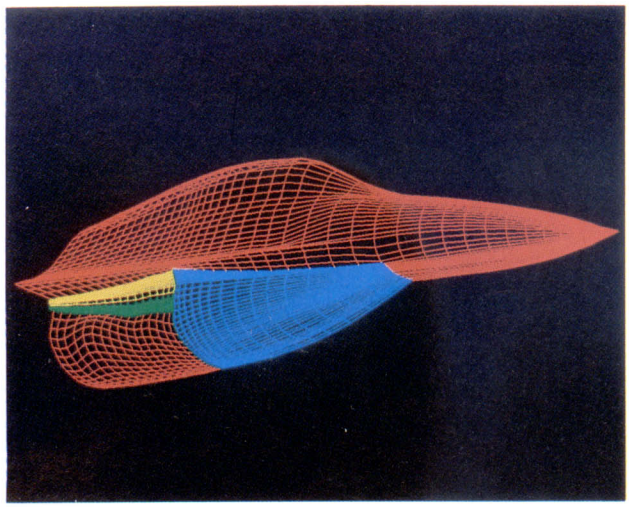

Fig. 4 Outer boundary grids of inlet-diverter section.

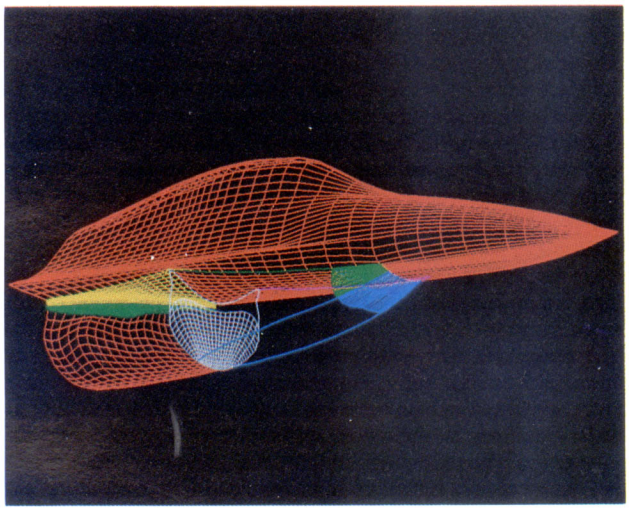

Fig. 5 Inlet-diverter grids highlighted.

boundaries separating zone 1 from the inlet and diverter (or inner) zones. These boundaries do not overlap, as do most of the other zones, but rather are coincident. With 19 zones, there are approximately 350,000 grids points. The inviscid zones away from the geometry have as little as 5000 grid points, while the viscous grid dimensions range from 25,000 to 37,000 grid points.

Figure 5 gives a better illustration of the inner grids. The inlet grid has a grid singularity where it collapses onto the fuselage; however, no-slip conditions are applied there. The end of the inlet grid is denoted by white, and two different types of boundary conditions are applied there. For now, flow-through inlet conditions are applied, i.e., boundary values at the inlet face are determined by extrapolation for the computed solution values for one plane upstream of the inlet face. (This type of boundary value at the inlet face does not account for any spillage that occurs from the inlet.) Above the inlet face, averaging (from the inlet and diverter regions) and interpolation procedures are combined to supply the boundary values at this plane. No-slip conditions are applied at the underbelly of the fuselage as well as symmetry conditions along the plane on which the diverter lies. The outer boundary, denoted by the blue lines, are updated by averaging (from zone 1 and the inlet zone) and interpolation routines. Similar averaging, from the diverter grids to both zone 1 and the inlet grid, along with interpolation routines, update the outer boundaries of the lower diverter (green) grid, and the upper diverter (yellow)

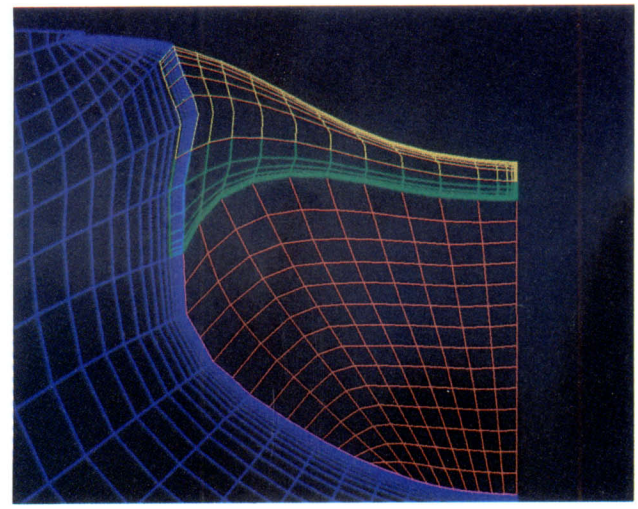

Fig. 6 Cross-section through diverter region.

grid. No-slip boundary conditions are applied at solid surface boundaries of the diverter grids.

Figure 6 illustrates a cross section through the fuselage at a streamwise location that coincides with the face of the inlet. Zone 1 is denoted by the dark blue grid, the inlet face by the color red, the upper diverter zone by the color yellow, and the lower diverter zone by the color green. Notice that the inlet grid and zone 1 do not overlap but coincide at a single boundary. Initially, this was also the case for the diverter zones and zone 1. However, simple averaging across this type of boundary, where one grid is coarse and the other grid is finely clustered, creates problems not only in convergence but also produces large flow gradients at these boundaries. This type of approach was taken since it was the easiest to implement into the existing flow solver. However, due to the poor results, overlapping was incorporated between the diverter grids and zone 1. As can be seen in Fig. 6, the diverter grids overlap zone 1 by about eight cells. This amount of overlap was chosen since one cell of the diverter zone approximately equals eight cells of zone 1. There has been no study to determine whether this is an optimal number of overlapping cells for convergence and quality of results. However, this overlapping did improve the quality of the results around this region. Updating the interfaces between the inlet and diverter zones and the inlet zone and zone 1 was still accomplished by using simple averaging and interpolation.

### Zonal Boundary Conditions

Communication between the blocks is achieved by means of an interpolation procedure. First the grid zones are carefully (but automatically) constructed so as to overlap by a specific number of cells (usually one or two). Then, information required at the edge of one zone is interpolated from the interior of another zone. This situation is illustrated in Fig. 7a. The boundary of zone 2, the ABCD plane, is updated after zone 1 has been advanced one time step. Notice that certain grid points are fixed to automatically coincide (Fig. 7b), so that the interpolation of information from zone 1 to zone 2 is easily accomplished. For the results presented herein, simple linear interpolation in the $\zeta$ and $\eta$ directions was used. The updating of boundary conditions for zone 1 is even more easily accomplished. Since zone 1 is coarse relative to zone 2, and certain points have automatically been fixed to coincide with zone 2, the transfer of information to zone 1 is via simple injection.

## Results

The case computed was for flow conditions of $M_\infty = 0.9$ and $\alpha = 4.12$ deg, and a Reynolds number of $4.5 \times 10^6$ based on root chord. Figures 8a and 8b indicate the wing pressure distri-

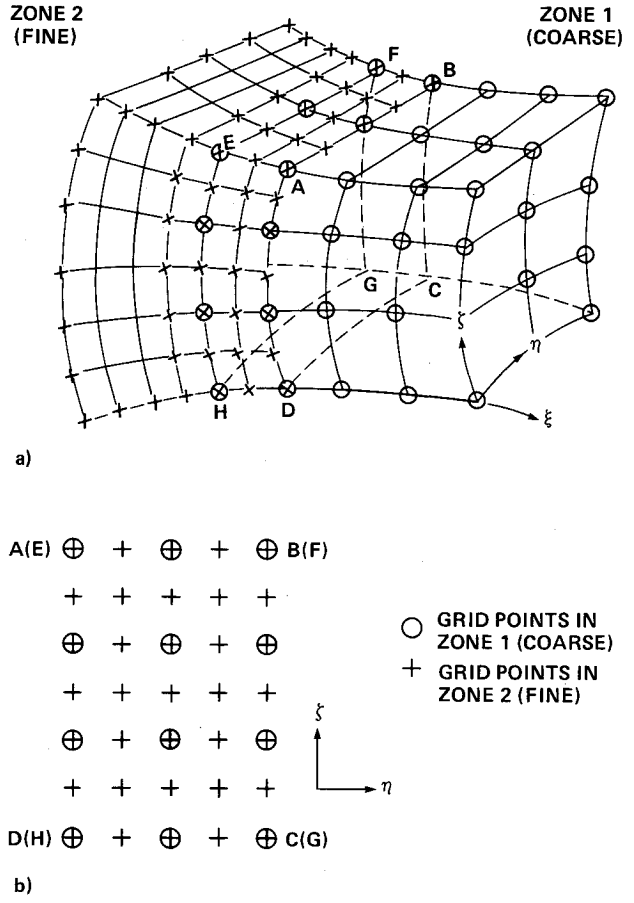


**Fig. 7 Two-zone overlapping scheme: a) two-zone grid showing overlap at ABCD and EFGH planes in physical space; b) grid point detail in overlap region in transformed space.**

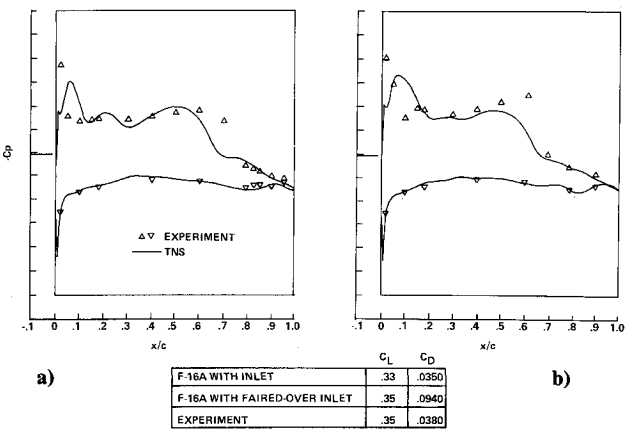


| | $C_L$ | $C_D$ |
|---|---|---|
| F-16A WITH INLET | .33 | .0350 |
| F-16A WITH FAIRED-OVER INLET | .35 | .0940 |
| EXPERIMENT | .35 | .0380 |

**Fig. 8 Comparison of wing pressure coefficients: $M_\infty = 0.9$, $\alpha = 4.12$ deg, $Re_c = 4.5 \times 10^6$; a) $\eta = 0.71$; b) $\eta = 0.84$.**

bution compared against experimental data[26] for different spanwise stations. Most of the experimental data available was in the form of pressure distributions. Some oil-flow data were available for the wing surfaces and were compared with a simulated oil pattern in a previous paper.[21] Unfortunately, no oil-flow or boundary-layer data exist around the inlet region, to the best of the authors' knowledge. In some cases the spanwise distance for the grid and experiment matched, and in other cases they were offset by a few inches. Figure 8a is for a spanwise location of $\eta = 0.71$. At the leading edge of the wing, the computations tend to underpredict the pressure. This, in fact, occurs across the entire wing. This underprediction is because of the lack of resolution at the leading edge of the wing. There are 60 points on the upper surface of the wing in the streamwise direction. Proceeding outboard, the resolution improves because of the tapering of the F-16A wing. At this spanwise station, there is sufficient grid resolution such that the shock can be clearly seen. More inboard of this span-station, capturing of the shock becomes more difficult due to poor streamwise resolution. The lower surface pressures match fairly well, and the upper surface, with the development of the shock, matches fairly well over most of the chord. The location of the shock with the computations is off by about 5 to 10%; however, the flow calculations capture the peak pressure of the shock very well. For a spanwise location of $\eta = 0.84$ (Fig. 8b), good prediction of pressure occurs again on the lower surface. The upper surface comparison is also fair, with the peak pressure at the shock being underpredicted. However, the pressure after the shock and the shock location are in good agreement. Recently, for the faired-over inlet case, this same case was rerun with twice as many points in the streamwise direction. This resulted in a favorable improvement with the comparison between the computed result and experiment.[21] The shock on the inboard portions of the wing began to develop, and it is anticipated that more resolution would tend to sharpen the shock. It should be noted that the Baldwin-Lomax equilibrium turbulence model is used for the results contained herein. However, numerical experiments conducted on the TNS wing-alone code,[27] indicate that a nonequilibrium turbulence model will have only a small effect on the pressure distribution.

A comparison of $C_L$ and $C_D$ for the computations vs experiment is given in Fig. 8. The experimental value of lift is for a flow-through inlet and no tail assembly. In the initial computations with the faired-over inlet, the favorable comparison of the numerical and experimental $C_L$ was fortuitous. However, on examining the wing pressure distributions, due to the failure to capture exactly the shock strength and position, the computations underpredicted the lift resulting from the wing surfaces alone. Fortunately, the inlet fairing added enough positive lift to match the experimental data. Now, with the computed inlet solution, it can be seen that about 0.02 of lift was generated by the inlet fairing. This is the correct trend and it indicated the necessity for better resolution on the wing to properly match the lift coefficient.

The experimental drag coefficient has a value of 380 counts as can be seen from the table. The drag due to the faired-over inlet case was off by a factor of 3. This was a result of the large stagnation region experienced by the inlet fairing. The drag count due to the inclusion of the inlet region is now 350. This is good, considering that this does not include any drag due to the tail assembly. The experimental drag of 380 counts includes the tail assembly, unlike the lift that did not include the tail assembly. The tail assembly, if scaled to the wing-root chord, would add 20–30 counts of drag indicating the proper trend in the calculated drag count.

Figures 9a–9c present cross-sectional $C_P$ comparisons between the computed solution and experiment for the inlet regions. Figure 9a gives a comparison at a streamwise location of $\xi = 0.14$ for both experiment and the computed results. (Note that $\xi = 0.0$ corresponds to a streamwise location coincident with the inlet face, and $\xi = 1.0$ indicates the streamwise location where the diverter ends.) The triangles are experimental results, the solid line shows the computed results, and the dashed line is the cross-sectional body definition, showing the inlet, diverter section and the leading-edge strake. Proceeding around the inlet area, the computations underpredict the pressure compared to the experimental values. However, this close to the inlet face, spillage occurs that tend to accelerate the flow. The reason for the underprediction of the $C_P$ around the inlet is due to the fact that very little, if any, spillage occurs from the inlet. This is because of the boundary conditions at the inlet face. The grid does not extend into the inlet itself and one-point extrapolation determines the inlet mass flow rate. Spillage that would normally occur would tend to accelerate the flow around

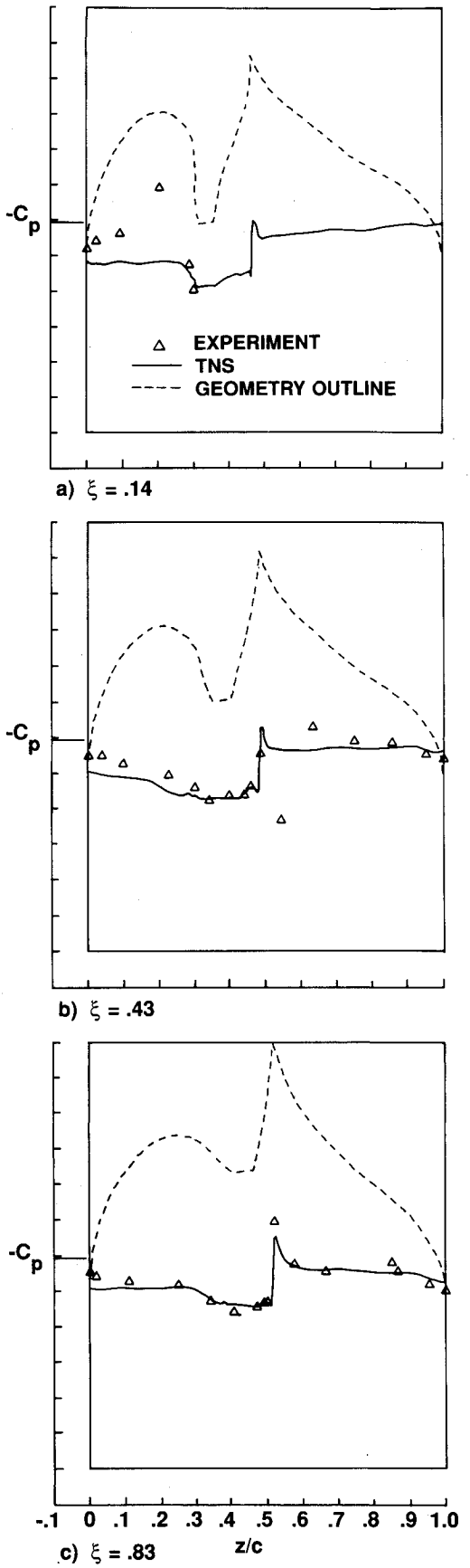


**Fig. 9 Comparison of inlet-diverter pressure coefficients: $M_\infty = 0.9$, $\alpha = 4.12$ deg, $Re_c = 4.5 \times 10^6$; a) $\xi = 0.14$; b) $\xi = 0.43$; c) $\xi = 0.83$.**

the inlet and increase the $C_P$. The computations, with the current boundary conditions, insure that no spillage occurs. However, it should be pointed out that in free-flight conditions, the design conditions would actually favor no possible spillage. The comparisons in the diverter section are in very good agreement.

At $\xi = 0.43$, the computations tend to underpredict the experimental pressure coefficient values at the lower area of the inlet (Fig. 9b). Proceeding around the inlet and into the diverter section, the computed results indicate an increase in pressure coefficient, followed by the deceleration of the flow at the diverter plate, as indicated by experiment. The computations indicate a slight acceleration approaching the strake. The $C_P$ then gradually climb after the strake near the top of the fuselage. Again the experimental $C_P$ are underpredicted after the strake location. The underprediction in the wraparound direction, outside of the inlet, is due to insufficient resolution, as shown in Ref. 21. However, the comparison of the $C_P$ in the diverter area itself is in very good agreement.

Figure 9c shows a comparison at a streamwise location of about $\xi = 0.83$. Again the $C_P$ on the lower portion of the inlet is slightly underpredicted. As the diverter section is approached, the computed solution indicates a higher pressure value. The computed solution fails to pick up the peak $C_P$, around the strake area. From the strake region to the top of the fuselage, there is fair agreement with experiment. In general, the wing pressure field is not significantly affected by the complex interaction that seems to be occurring around the inlet region. Again, the comparison in the diverter area itself is very good. This is somewhat surprising, since the Baldwin-Lomax model that is applied in this region is really not the appropriate type of turbulence model to use. It would be expected that the entire flow in the diverter area is turbulent and fully developed and would resemble channel flow more than boundary-layer flow. However, for a first of a kind calculation on a very complicated geometry, the results are encouraging. This solution required about 3000 iterations, at a data processing rate of 36 $\mu$s per iteration per grid point. For the current grid, this required about 10 h of CPU time on the Cray X-MP/48. More work is needed in the interpolation routines used in transferring information from the inlet grids to the "outer" grids, specification of the mass flow at the inlet face, and more streamwise resolution on the wing. Future work will try to concentrate on these matters as well as inclusion of the tail assembly.

Figure 10 illustrates pressure contours around the lower diverter region. The black line indicates the boundary between the lower diverter and the outer grids. In our initial calculations, no overlapping of the zones was used. This resulted in the buildup of gradients centered at the zonal boundaries, as can be seen in the figure. Figure 11 is the case where overlapping of the zones was used and the gradient buildup no longer occurs. The pressure contours pass smoothly between the two zones. The flow features in this region are intuitively correct, including a stagnation region at the lip of the inlet and the acceleration of the flow over the inlet region. There also appears to be a spanwise pressure gradient from the diverter region outward. Overlapping of the zones between the inlet and diverter grids still remains to be done, as can be evidenced by the gradient buildup of pressure around the inlet lip region.

Figure 12 illustrates the pressure contours on the upper diverter region. Again, it can be seen that the pressure contours pass smoothly to the outer zone and from the upper to lower diverter zones.

Figure 13 is a simulated oil-flow pattern on the lower diverter surface. Particle traces are released at every other streamwise location beginning at the inlet lip, and every spanwise station beginning from the diverter plate. These traces are restricted to the computational plane one grid point off the geometry surface. It can be seen from these traces that there exists a strong gradient in the spanwise direction. The strength of this pressure gradient diminished as the traces proceed downstream. Particles released near the lip and diverter plate proceed in a spanwise direction until the traces are influenced by the outer flow and then are abruptly twisted and entrained

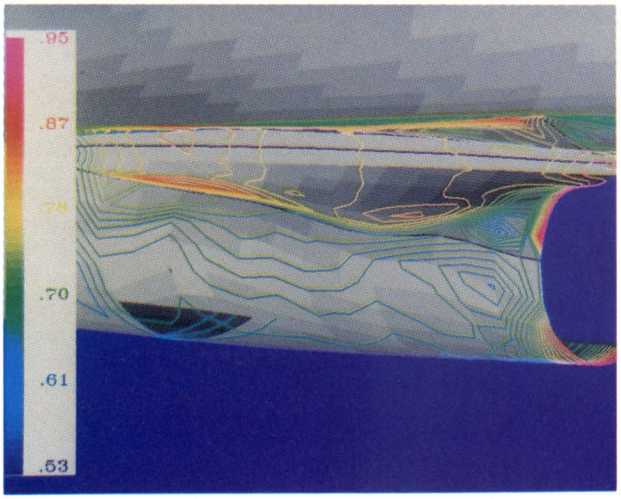


Fig. 10 Pressure contours on lower diverter region (without overlapping of diverter and outer grid).

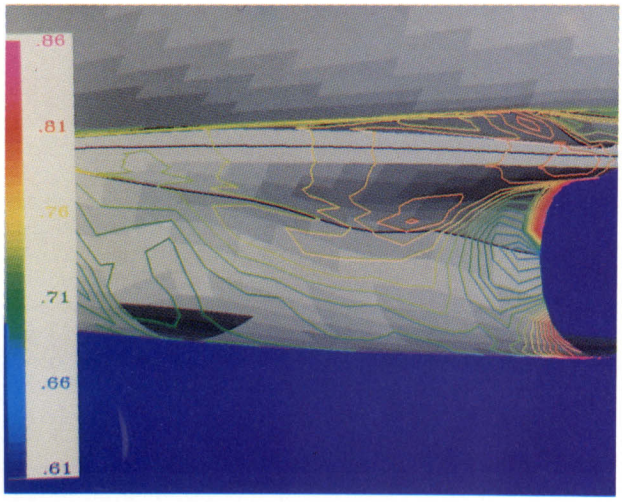


Fig. 11 Pressure contours on lower diverter region (with overlapping of diverter and outer grid).

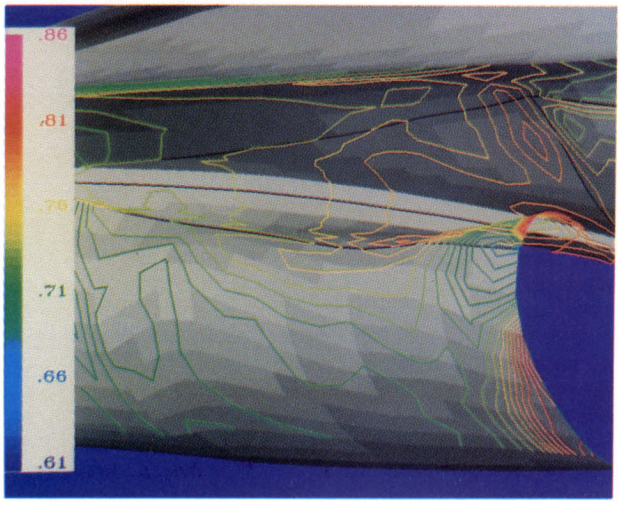


Fig. 12 Pressure contours on upper diverter region.

in the outer streamwise flow. [It should be pointed out that the apparent discontinuity between the particle traces that are in the diverter region and those that are on the side of the inlet (zone 1) is due to the plotting routine. The lower diverter plane corresponds in computational space to an $i$-$j$ plane, whereas the side of the inlet (zone 1) corresponds to a $j$-$k$ computational plane. The plotting routine cannot maintain continuity of particle traces across two different types of computational planes.] A separation line appears near the lip of the inlet and the boundary between zone 1 and the diverter zone. Boundary layer profiles of the $u$ component of velocity through this region do, in fact, indicate reverse flow.

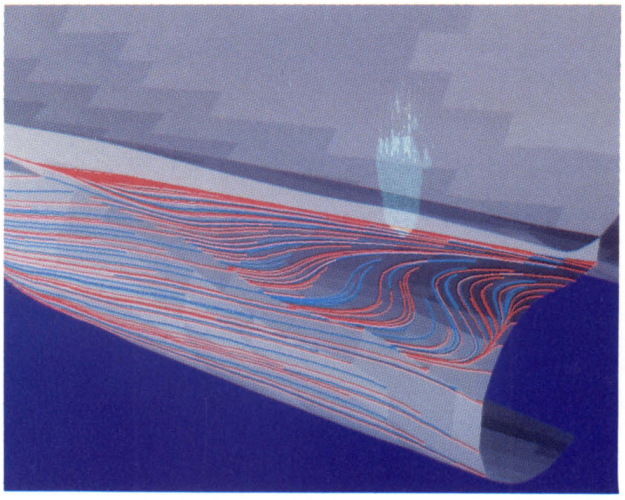

Fig. 13 Simulated oil-flow on lower diverter surface.

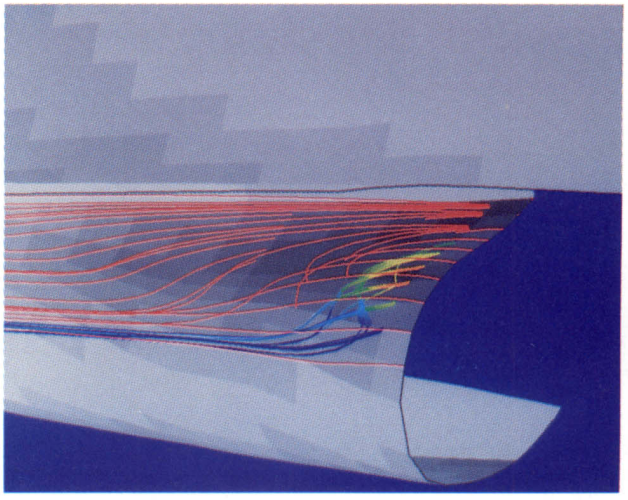

Fig. 14. Particle traces around inlet region.

Figure 14 illustrates particle traces released around the separated region that are not confined to any computational surface. The particles released at the inlet lip and near the diverter plate were colored red. The traces from the diverter region head downstream with some influence of the spanwise pressure gradient indicated. The particle traces near the separation region, which were released at the lip of the inlet, go up and over what appears to be a separation bubble. More particle traces released in the separation region itself are colored according to elevation in the $z$-direction. This was done in an effort to better visualize the flow. It appears that the particles closer to the diverter, and at a higher elevation, head in a spanwise direction and proceed under those particles released farther outboard. Eventually, all these particles are entrained in the outer fluid at about the same elevation level and are swept downstream.

## Conclusions

The TNS code has been extended to compute the transonic viscous flow over the F-16A configuration including inlet. The TNS code uses a zonal approach, which allows appropriate clustering on all aircraft surfaces, a task extremely difficult for a single grid. Pressure contours indicate the continuity of the

flow across these zonal boundaries. The thin-layer Navier-Stokes equations are solved in the viscous regions, and the Euler equations are solved in the inviscid regions. The code also allows for easy modification to increase the number of zones or to refine existing zones for additional grid resolution where it is needed. Computations for a transonic turbulent case require about 3000 iterations, or about 10 h of CPU time on the current NASA Ames supercomputer. Pressure distributions at various span stations on the wing and at cross sections through the inlet compare favorably with those of experiment.

## Acknowledgment

The authors would like to acknowledge the work of Jason Williams, who is instrumental in the TNS project, and who produced the color graphics contained in this paper.

## References

[1]Holst, T. L., Tannehill, J. C., and Rakich, J. V., "Numerical Computation of Viscous Blunt Body Flows with Planar Impinging Shock," NASA SP-347, 1975, pp. 1457–1471.

[2]Hung, C. M., "Numerical Solution of Supersonic Laminar Flow over an Inclined Body of Revolution," AIAA Paper 79-1547, July 1979.

[3]Hung, C. M., "Impingement of an Oblique Shock Wave on a Cylinder," AIAA Paper 82-0025, Jan. 1982.

[4]Shang, J. S., "Numerical Simulation of Wing-Fuselage Aerodynamic Interaction," AIAA Paper 83-0225, Jan. 1983.

[5]Pulliam, T. H. and Steger, J. L., "Implicit Finite Difference Simulations of Three-Dimensional Compressible Flows," AIAA Paper 78-0010, Jan. 1978.

[6]Deiwert, G. S. and Rothmund, H., "Three-Dimensional Flow over a Conical Afterbody Containing a Centered Propulsive Jet: A Numerical Simulation," AIAA Paper 83-1709, July 1983.

[7]Deiwert, G. S., Andrew, A. E., and Nakahashi, K., "Theoretical Analysis of Aircraft Afterbody Flow," AIAA Paper 84-1524, June 1984.

[8]Fujii, K. and Kutler, P., "Numerical Simulation of the Viscous Flow Fields over Three-Dimensional Complicated Geometries," AIAA Paper 83-1098, Jan. 1983.

[9]Mansour, N. N., "Numerical Simulation of the Tip Vortex Off a Low-Aspect Ratio Wing at Transonic Speed," AIAA Paper 84-0522, Jan. 1984.

[10]Obayashi, S. and Kuwahara, K., "Navier-Stokes Simulation of Side Wall Effect of Two-Dimensional Transonic Wind Tunnel," AIAA Paper 87-0037, Jan. 1987.

[11]Fujii, K. and Obayashi, S., "Navier-Stokes Simulation of Transonic Flow over Wing-Fuselage Combinations," AIAA Paper 87-1831, Jan. 1987.

[12]Obayashi, S., Fujii, K., and Takanashi, S., "Toward the Navier-Stokes Analysis of Transport Aircraft Configurations," AIAA Paper 87-0428, Jan. 1987.

[13]Chapman, D. R., "Computational Aerodynamics: Review and Outlook," *AIAA Journal*, Vol. 17, Dec. 1979, pp. 1293–1313.

[14]Atta, E. H., "Component-Adaptive Grid Interfacing," AIAA Paper 81-0382, Jan. 1981.

[15]Atta, E. H. and Vadyak, J. A., "Grid Interfacing Zonal Algorithm for Three-Dimensional Transonic Flows About Aircraft Configurations," AIAA Paper 82-1017, 1982.

[16]Hessenius, K. A. and Pulliam, T. H., "A Zonal Approach to Solution of the Euler Equations," AIAA Paper 82-0969, June 1982.

[17]Rai, M. N., "A Conservative Treatment of Zonal Boundaries for Euler Calculations," AIAA Paper 84-0164, Jan. 1984.

[18]Chaderjian, N. M. and Steger, J. L., "A Zonal Approach for the Steady Transonic Simulation of Inviscid Rotational Flow," AIAA Paper 83-1927, June 1983.

[19]Flores, J., Holst, T. L., Kaynak, U., Gundy, K., and Thomas, S. D., "Transonic Navier-Stokes Wing Solution Using A Zonal Approach: Part I. Solution Methodology and Code Validation," AGARD Paper 30A, April 1986.

[20]Flores, J., "Convergence Acceleration for a Three-Dimensional Euler/Navier-Stokes Zonal Approach," AIAA Paper 85-1495, July 1985.

[21]Flores, J., Reznick, S. G., Holst, T. L., and Gundy, K., "Navier-Stokes Solutions for a Fighter-Like Configuration," AIAA Paper 87-0032, Jan. 1987.

[22]Reznick, S. G. and Flores, J., "Strake-Generated Vortex Interactions For A Fighter-Like Configuration," AIAA Paper 87-0589, Jan. 1987.

[23]Eberle, A., "Euler Solution for a Complete Fighter Aircraft Configuration at Sub- and Supersonic Speed," AGARD Paper 17, April 1986.

[24]Karman, S. L., Steinbrenner, J. P., and Kisielewski, K. M., "Analysis of the F-16 Flow Field by a Block Grid Euler Approach," AGARD Paper No. 18, April 1986.

[25]Sorenson, R. L., "Three-Dimensional Elliptic Grid Generation About Fighter Aircraft for Finite-Difference Solutions," to be published as a NASA Technical Memorandum.

[26]Reue, G. L., Doberenz, M. E., and Wilkins, D. D., "Component Aerodynamic Load from 1/9-Scale F-16A Loads Model," General Dynamics Fort Worth, TX, Rept. 16PR316, May 1976.

[27]Kaynak, U. and Flores, J., "Advances in the Computation of Transonic Separated Flows over Finite Wings," AIAA Paper 87-1195, June 1987.